J Intel Connect Veh

Research Article

Are Smartphones Viable for the V2X Transition? A Platoon-Perspective Stability Analysis under Real-World Errors

Baofeng Sun[1,✉], Wenyu Yang[1,✉], Guodong Ma[1,✉], Xiaoxiang Na[2]

Cite this article: https://doi.org/10.26599/JICV.2026.9210106

ABSTRACT: The benefits of vehicle-to-everything (V2X) systems remain limited by the large stock of conventional vehicles, low penetration, and high retrofit cost. From a platoon perspective, this paper evaluates smartphones as low-cost transitional V2X terminals. Because data accuracy is the main barrier to large-scale smartphone use, we collected 12 h of onboard reference data and 72 h of smartphone observations across three road scenarios, three smartphone vendors, and two device generations. We then analyzed the statistical characteristics of smartphone GNSS speed errors. The errors were well described by a three-component Laplace mixture model. Their main body consisted of two small-magnitude components and was accompanied by low-probability heavy-tailed errors. Based on the measured error characteristics, we developed a linear stochastic platoon dynamics model for connected human-driven vehicles (CHVs) and derived mean-square stability conditions to evaluate the stability applicability boundary of low-cost V2X. The results show that the current measured error parameters retain a good stability margin over the common driving speed range, and the occurrence probability and scale of the heavy-tailed component are the main factors affecting the strict mean-square stability boundary. Monte Carlo simulations further show that, under empirical full mixture errors, the average improvement in stability performance relative to the human-driven vehicle baseline reaches 75.84%, whereas the degradation relative to the ideal CHV case is only 1.79%. These results indicate that smartphones used as V2X terminals have the potential to improve platoon stability through vehicle state sharing. They provide a quantitative basis for transitional V2X deployment among existing vehicles.

KEYWORDS: connected human-driven vehicle (CHV); perceptual uncertainty; car-following model; mean-square stability

Just Accepted

1 Introduction

Vehicle-to-everything (V2X) is a core technology for next-generation intelligent transportation systems. It has strong potential to improve road safety and traffic efficiency(Dong et al., 2022; Sun et al., 2023; Wu et al., 2024; Oh et al., 2026; Ma et al., 2026b; Jiang et al., 2026; Ma et al., 2026a). In recent years, V2X deployment has accelerated worldwide. By the end of 2025, more than 500,000 passenger cars in China had been factory equipped with cellular V2X (C-V2X) modules(Research In China, 2025). The United States has also launched several V2X pilot deployments in cities such as Detroit and Tampa(U.S. Department of Transportation, 2024). However, despite this promise, the practical benefits of V2X in current traffic environments are still strongly limited by penetration. Existing studies show that the improvement brought by V2X begins to emerge when the penetration rate reaches 60%(Cui and Yu, 2025). Its system-level advantages become significant only when the penetration rate exceeds 80%(Qin and Wang, 2021). Compared with China's 469 million motor vehicles, the current effective penetration rate in the traffic system remains below 1%.

Unlike new vehicles delivered with an onboard unit (OBU), existing conventional vehicles face high retrofit costs when they are connected to a V2X network(Jing et al., 2022; Zimmer et al., 2024; Gu et al., 2026). A typical aftermarket V2X module must include three functional units: vehicle state acquisition, data processing, and wireless communication(Meneguette et al., 2023). In practice, a conventional vehicle needs an automotive-grade processing unit and a communication module. It must also obtain real-time state information in one of two ways. The first is to directly integrate high-precision GNSS/RTK hardware(D. Lee et al., 2021; Lusvarghi et al., 2023; Xia et al., 2023). The second is to install a standard GNSS module and modify the CAN bus or OBD-II wiring, so that vehicle states can be extracted through multisource data fusion(Ge et al., 2018; Arena et al., 2019; Wang et al., 2023; J.W. Lee et al., 2025). According to public procurement data from Zhejiang Province, China, the average cost of retrofitting one vehicle with C-V2X is about 3710 RMB(China Government Procurement Network, 2026). Based on the vehicle stock noted above, achieving a penetration rate above 60% would require more than 1 trillion RMB, or about 150 billion USD. This is economically challenging. Therefore, a low-cost and smooth transitional scheme is important for the gradual adoption of V2X technology.

To address this bottleneck, previous studies have proposed using smartphones as in-vehicle V2X terminals(Hadiwardoyo et al., 2018; Lim et al., 2021; Speiran and Shakshuki, 2022). From the perspectives of hardware capability and application ecosystem, this idea is already practically feasible to some extent. Smartphone computing power is sufficient for data processing. At the same time, free navigation services such as Amap and Baidu Maps, as well as ride-hailing platforms such as Didi, are widely used. Smartphones therefore have a high presence rate and activity level during vehicle travel(iiMedia Research, 2024). Civil-grade sensors built into smartphones cannot fully match automotive-grade OBUs. Objective gaps remain in communication range, information timeliness, and measurement accuracy(Abdel-Aty et al., 2020). Even so, the application environment for smartphones as

[1] School of Transportation, Jilin University, Changchun 130022, China. [2] Department of Engineering, University of Cambridge, Cambridge CB2 1PZ, UK.

✉ Corresponding author. E-mail: B. Sun, sunbf@jlu.edu.cn; W. Yang, yangwy24@mails.jlu.edu.cn; G. Ma, magd22@mails.jlu.edu

Received: July 28, 2026; Revised: September 15, 2026; Accepted: October 5, 2026

© The Author(s) 2026. This is an open access article under the terms of the Creative Commons Attribution 4.0 International License (CC BY 4.0, http://creativecommons.org/licenses/by/4.0/).

V2X terminals is becoming increasingly mature. At the communication level, C-V2X has become the mainstream technical route as protocols have evolved. Smartphones can directly access the V2X system through LTE/5G networks via the Uu interface. This overcomes the communication range limitations of early schemes, such as Wi-Fi based DSRC emulation(Liu et al., 2016; Hadiwardoyo et al., 2018). In addition, previous work has shown that, even under relatively large communication delay (over 0.1 s), traffic flow composed of connected human-driven vehicles with beyond-line-of-sight perception still performs better than conventional traffic flow. Such capability is valuable in noncritical safety scenarios, including beyond-line-of-sight warnings, capacity improvement, and mitigation of phantom traffic jams(Yang et al., 2026). On this basis, this paper regards smartphones as low-cost connected terminals for existing conventional vehicles. The goal is to share vehicle states through cellular networks and provide conventional vehicles with some beyond-line-of-sight perception. Therefore, determining whether smartphones can provide effective stability benefits to traffic systems under civil-grade sensor accuracy is a prerequisite for assessing the feasibility of large-scale deployment.

To evaluate the influence of accuracy limitations on traffic systems, researchers often build platoons using continuous stochastic car-following models(Fei et al., 2023; Liang and Pang, 2024; Long et al., 2024). Stability analysis is then used to characterize the propagation of perturbations through the platoon, which reveals the benefits of different error levels in disturbance suppression and roadway capacity improvement. Within this framework, previous studies have examined how errors affect system benefits for different vehicle types. These studies can be roughly divided into two groups according to how the errors are represented. The first group focuses on constant bias, where the error is treated as a fixed offset to analyze the influence of perception or control bias on the equilibrium state and stability boundary. Examples include the analyses by S. Li et al. (2023, 2024a, 2024b, 2024c) and Zhou et al. (2025) on errors in autonomous vehicles and connected automated vehicles. The second group focuses on random fluctuations, where the error is treated as a zero-mean disturbance around the true value. This representation is used to describe the effects of communication noise, perception uncertainty, or measurement errors on vehicle responses. Examples include Bouadi et al. (2022) for human-driven vehicles, Sun et al. (2023) and Sui et al. (2024) for communication-related errors in connected vehicles, and H. Li et al. (2025) and Zhao et al. (2025) for connected automated vehicles. These studies provide a basis for evaluating the impact of smartphone errors on traffic systems. However, actual smartphone vehicle state perception errors may have more complex statistical characteristics. They are difficult to describe using only a constant error or a single zero-mean random noise term. If only these simplified representations are used, stability analysis cannot reflect the applicability boundary of low-cost V2X terminals in real traffic. It is therefore necessary to derive mean-square stability conditions based on measured error distributions while considering both error mean and fluctuation.

To address these limitations, this paper obtains measured smartphone vehicle state perception errors and their distributional characteristics through real-vehicle experiments covering multiple road scenarios, smartphone vendors, and device generations. The measured errors are then introduced into a CHV platoon model with V2X errors. Stability conditions that consider both the error mean and fluctuation intensity are derived to evaluate the applicability boundary and application potential of smartphones as low-cost V2X terminals at the platoon level.

The main contributions of this paper are as follows:

1) For applications in which smartphones serve as low-cost V2X terminals, smartphone data were collected from real-vehicle experiments across multiple scenarios, vendors, and device generations. The distributional structure of smartphone GNSS speed errors was identified.

2) Based on the measured error distribution, mean-square stability conditions considering both error mean and fluctuation intensity were derived. The stability boundaries and their evolution under current error levels were then obtained analytically.

3) Monte Carlo simulations were conducted to compare small error, tail error, and empirical full mixture regimes. These simulations quantitatively evaluated the improvement in platoon stability provided by low-cost V2X under different tail characteristics.

The remainder of this paper is organized as follows. Section 2 identifies the distributional characteristics of smartphone vehicle state perception errors through real-vehicle experiments. Sections 3 and Sections 4 construct the linear stochastic platoon dynamics and derive the mean-square stability conditions. Section 5 evaluates disturbance propagation and system improvement through Monte Carlo simulations. Section 6 concludes the paper and outlines future research directions. The appendices provide details of the error measurements and characteristic analysis, as well as the distribution fitting procedure.

2 Error Measurement and Characteristic Analysis

To quantify the accuracy difference between civil-grade smartphone sensors and automotive-grade sensors, this section presents real-vehicle experiments in typical traffic scenarios. Raw sensor data were collected from smartphones of different vendors and generations. Measurements from high-precision onboard equipment were used as the reference, and the error distribution characteristics were then analyzed statistically.

2.1. Experimental Design and Data Collection

Fig. 1 shows the data acquisition hardware setup of the experimental platform. Two test vehicles, a Volkswagen Golf and a Volkswagen Passat, were used. Each vehicle was equipped with a UM982 RTK-GNSS receiver and an ELM327 OBD-II module to obtain high-precision positioning and vehicle operating state data. To cover different road operating environments, highways, urban expressways, and urban roads were selected as three typical traffic scenarios. Each vehicle was driven for 2 h in each scenario, producing 12 h of reference data in total. To account for vendor and generation differences, six recent and earlier models from Apple, Samsung, and Xiaomi, which rank among the leading global smartphone vendors, were selected as terminals. GNSS, IMU, and other sensor data and device status information were

Just Accepted

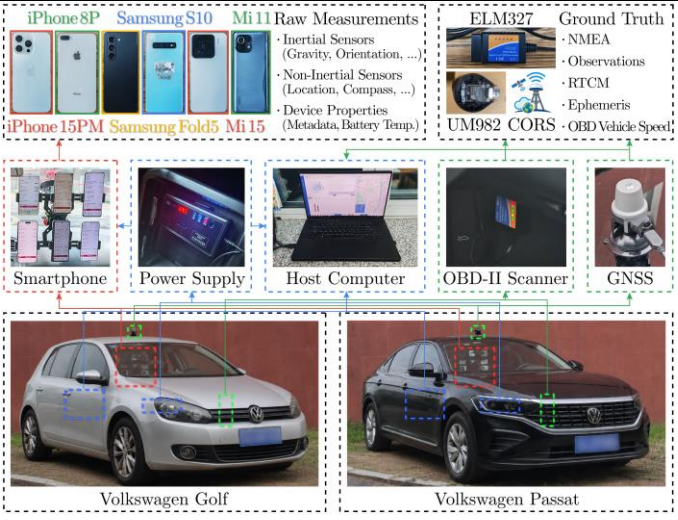

Fig. 1. Data Acquisition Hardware Setup

recorded synchronously. All smartphones used the Sensor Logger app for unified data collection. Multisource synchronization was achieved using timestamps calibrated by a network time protocol server. In total, 72 h of smartphone observations were collected, providing data support for subsequent error statistics and model construction. Detailed experimental conditions and data information are provided in Appendix A.

2.2. Ground-Truth Construction and Error Extraction

Although the smartphones collected multisensor data, including GNSS and IMU measurements, this paper evaluates only the raw GNSS speed field. This choice is made because common V2X schemes mainly use GNSS as the input, and integrated navigation algorithms may introduce additional uncertainty. The ground-truth velocity was constructed as follows. The onboard RTK horizontal velocity was used as the main curve, and abnormal points were removed according to the solution status and self-reported standard deviation. The OBD-II speed curve was then introduced under dry road conditions during data acquisition. It was used to match the dynamic trend near abnormal segments and to interpolate a continuous ground-truth sequence. For smartphone data processing, GNSS points with abnormal self-reported accuracy were first removed using hard thresholds. To avoid dilution of dynamic errors by steady data in constant-speed phases, only acceleration and deceleration data were retained according to relevant standards(Ministry of Industry and Information Technology of the People's Republic of China, 2019), with $v \geq 0.5\text{km/h}$ and $|a| > 0.15\text{m/s}^2$. Before error extraction, cross-correlation analysis was used to eliminate time-lag bias between data sources. The smartphone velocity and the ground truth were then sampled at a fixed frequency, and their difference formed the discrete speed error dataset. Following previous GNSS error modeling studies(Teunissen, 2020; Duong et al., 2021; Specht, 2021; Yan et al., 2025), distribution fitting was performed under different aggregation dimensions. The results show that the three-component Laplace mixture model (LMM-3) gives the best fit. Details are provided in Appendix B.

2.3. Error Distribution Characteristics Analysis

To identify the main factors affecting smartphone V2X speed errors, this subsection fits the LMM-3 model by scenario, vendor, and device generation. The results are shown in **Table 1.** Components 1, 2, and 3 in the table correspond to the three Laplace components of LMM-3. π_i is the mixing weight of component i and represents its relative occurrence probability. μ_i is the location parameter and characterizes the error center and direction of bias. λ_i is the scale parameter and represents the fluctuation level of the component, with a larger value indicating a more

Table 1. Data Architecture and Distribution Fits of Speed Errors under Different Aggregation Dimensions

Dimension	Category	Component 1			Component 2			Component 3			Sample Composition
		π_1	μ_1	λ_1	π_2	μ_2	λ_2	π_3	μ_3	λ_3	
Scenario	Highway	0.480	-0.067	0.248	0.431	0.068	0.309	0.089	-0.229	1.170	2 Vehicles × 3 Vendors × 2 Generations
	Expressway	0.517	0.081	0.404	0.405	-0.102	0.321	0.078	-0.206	1.978	
	Urban Road	0.568	-0.097	0.296	0.340	0.096	0.250	0.091	-0.390	1.394	
Vehicle	VW Golf	0.490	-0.085	0.274	0.401	0.089	0.307	0.109	-0.232	1.309	3 Scenarios × 3 Vendors × 2 Generations
	VW Passat	0.633	-0.079	0.371	0.309	0.078	0.252	0.058	-0.222	1.994	
Vendor	**Apple** iPhone 15PM (2023) iPhone 8P (2017)	0.456	-0.110	0.410	0.388	0.121	0.388	0.156	-0.314	1.595	3 Scenarios × 2 Vehicles × 2 Generations
	Samsung Galaxy Fold5 (2023) Galaxy S10 (2019)	0.534	-0.089	0.252	0.444	0.051	0.203	0.022	-0.158	2.497	
	Xiaomi Mi 15 (2024) Mi 11 (2021)	0.549	-0.107	0.306	0.374	0.128	0.299	0.077	-0.169	0.997	
Generation	**Recent** iPhone 15PM (2023) Galaxy Fold5 (2023) Mi 15 (2024)	0.531	-0.095	0.316	0.427	0.103	0.323	0.042	-0.248	1.666	3 Scenarios × 2 Vehicles × 3 Vendors
	Earlier iPhone 8P (2017) Galaxy S10 (2019) Mi 11 (2021)	0.563	-0.076	0.315	0.300	0.064	0.234	0.137	-0.196	1.448	
Overall	All Data	0.583	-0.078	0.319	0.329	0.089	0.281	0.088	-0.210	1.519	Full Dataset

Note: All dimensions are fitted with LMM-3: $\sum_{i=1}^{3} \pi_i \mathrm{L}(\mu_i, \lambda_i)$. Parameters μ_i and λ_i are in km/h; π_i are dimensionless mixing proportions.

Just Accepted

dispersed distribution. The sample composition gives the combination of experimental objects covered by each row. Overall, the parameters under different dimensions show similar mixture distributions. The main body consists of two high-proportion components with small magnitudes and opposite directions, accompanied by a low-probability tail component with a larger magnitude. This pattern is consistent with previous findings on GNSS error distributions(Wen et al., 2021). It indicates that smartphone vehicle state perception errors have a relatively consistent main distribution across aggregation dimensions. Most errors are concentrated within a small-magnitude range, but the low-probability heavy-tailed risk cannot be ignored.

A further comparison across aggregation dimensions shows that the differences in error distributions are mainly reflected in the heavy-tailed characteristics. For road scenarios, the proportions of large-magnitude tail components are similar across environments. The main difference lies in fluctuation intensity, with the expressway scenario being the most prominent. This may be related to the joint influence of vehicle speed and the number of obstructions. For vehicle type, the two models show similar tail error contributions. Their difference is mainly a parameter compensation relationship between tail weight and fluctuation magnitude, rather than a clear change in the overall error level.

In contrast, vendor and generation have more evident effects on the error distribution. Apple devices show a clearly higher probability of large-component errors than Samsung and Xiaomi devices. Samsung devices have the lowest probability of large-component errors, but once such errors occur, their magnitude is the largest. Xiaomi devices show a more balanced error distribution. The generation comparison further shows that recent devices reduce the probability of abnormal large errors, but they do not fully eliminate heavy-tailed disturbances. This suggests that hardware generation improvement can suppress tail errors to some extent, but its capability remains bounded. Tail risk therefore still requires detailed analysis.

In summary, the main distribution of smartphone vehicle state perception errors is relatively consistent, but the low-probability heavy-tailed errors represented by Component 3 remain a potential risk. Their influence on the platoon system must therefore be further characterized. The subsequent simulations use the parameters of the Overall group in **Table 1** as the empirical full mixture input and focus on the influence of this tail component on the platoon system.

3 Modeling of Connected Human-Driven Platoons

In the low-cost V2X application scenario described in Section 1, existing conventional human-driven vehicles obtain vehicle state sharing and beyond-line-of-sight perception through smartphone terminals. In traffic systems, such human-driven vehicles with connected functions are defined as connected human-driven vehicles (CHVs). To evaluate the applicability boundary and application potential of low-cost V2X technology, this section introduces V2X error terms into the CHV car-following model framework based on the measured error characteristics. A corresponding homogeneous platoon model is then constructed.

Based on the CHV car-following model framework proposed by Yang et al. (2026), V2X error modeling is introduced to form a CHV car-following platoon with V2X errors. The acceleration $a_n(t)$ of any vehicle n in the platoon at time t is given by:

$$a_n(t) = a\left[1-\left(\frac{v_n(t-\tau_d)}{v_0}\right)^4-\left(\frac{s_n^*(\cdot)}{s_n(t-\tau_d)}\right)^2\right] \tag{1}$$

$$s_n^*(\cdot) = s_0 + Tv_n(t-\tau_d) + \frac{v_n(t-\tau_d)}{2\sqrt{ab}}\left(\Delta v_n^{(1)}(t-\tau_d)+\alpha_n \mathrm{D}(t)\tilde{X}_n(t)\right) \tag{2}$$

$$\mathrm{D}(t) = \left[1+\exp\left(-\kappa_n\left(\frac{s_n(t-\tau_d)}{\Delta v_n^{(1)}(t-\tau_d)}+\phi_n\right)\right)\right]^{-1} \tag{3}$$

where v_n is the vehicle velocity; s_n is the spacing; a is the maximum acceleration; v_0 is the desired velocity; s_0 is the minimum gap; T is the safe time headway; b is the comfortable deceleration; and τ_d denotes the driver reaction delay. $\Delta v_n^{(1)}(t-\tau_d)$ is the relative velocity with respect to the first preceding vehicle as perceived by the driver, namely $\Delta v_n^{(1)}(t-\tau_d) = v_n(t-\tau_d) - v_{n-1}(t-\tau_d)$. In addition, α_n is the maximum compliance rate. $\mathrm{D}(t)$ is the dynamic compliance regulation function, where $\mathrm{D}(t)=1$ when $\Delta v_n^{(1)}(t-\tau_d)\to 0^+$. κ_n and ϕ_n are sensitivity coefficients of this function. $\tilde{X}_n(t)$ is the V2X information stimulus term with errors. Considering the communication delay τ_c, it is defined as:

$$\tilde{X}_n(t) = \xi_n \sum_{m=2}^{M} \beta_m \Delta\tilde{v}_n^{(m)}(t-\tau_d-\tau_c) \tag{4}$$

where ξ_n is the sensitivity coefficient; M is the maximum communication topology depth of the V2X terminal; and β_m is the weighting factor for multiple preceding vehicles, satisfying $\sum_{m=2}^{M}\beta_m = 1$. $\Delta\tilde{v}_n^{(m)}(t-\tau_d-\tau_c)$ is the relative velocity with V2X error and delay:

$$\Delta\tilde{v}_n^{(m)}(t-\tau_d-\tau_c) = \Delta v_n^{(m)}(t-\tau_d-\tau_c) + \tilde{\eta}_n^{(m)}(t) \tag{5}$$

where $\Delta v_n^{(m)}(t-\tau_d-\tau_c)$ is the true relative velocity between the current vehicle and the m-th preceding vehicle, with $\Delta v_n^{(m)}(t-\tau_d-\tau_c) = v_n(t-\tau_d) - v_{n-m}(t-\tau_d-\tau_c)$. $\tilde{\eta}_n^{(m)}(t) \sim \sum_{i=1}^{3}\pi_i \mathrm{L}(\mu_i,\lambda_i)$ is the V2X error. According to the conclusion in Section 2, it follows the LMM-3 distribution.

Based on the actual characteristics of V2X terminals, the terminals are assumed to update information at a fixed interval Δt_e, with update instants denoted by $t_\ell = \ell\Delta t_e$. The measurement error $\tilde{\eta}_n^{(m)}[\ell]$ remains constant during the ℓ th update period:

$$\tilde{\eta}_n^{(m)}(t) = \tilde{\eta}_n^{(m)}[\ell], \quad t\in[t_\ell, t_{\ell+1}) \tag{6}$$

The subsequent strict mean-square stability analysis evaluates vehicle states at the V2X information update instants t_ℓ. For subsequent analysis, the error term is decomposed into a constant bias term and a zero-mean fluctuation term as follows:

$$\tilde{\eta}_n^{(m)}[\ell] = \bar{\mu} + \eta_n^{(m)}[\ell] \tag{7}$$

where $\bar{\mu} = \sum_{i=1}^{3}\pi_i\mu_i$ is the constant bias term, and $\eta_n^{(m)}(\ell)$ is the zero-mean fluctuation term, with $\sigma_\eta^2 = \sum_{i=1}^{3}\pi_i\left[2\lambda_i^2+(\mu_i-\bar{\mu})^2\right]$ and $\mathrm{E}\left[\eta_n^{(m)}(\ell)\right]=0$.

From the perspective of platoon-level feasibility assessment, this paper temporarily neglects spatiotemporal correlations among errors.

Table 2. Default Parameters of the Platoons

Parameter	Typical Value	Parameter	Typical Value
v_0	33.33 m/s	s_0	2.00 m
a	1.00 m/s^2	b	1.50 m/s^2
T	2.00 s	Δt_e	1.00s
τ_d	1.00 s	τ_c	0.50 s
ξ_n	0.50	α_n	1.00
κ_n	0.88	ϕ_n	-7.50
M	3	β_m	0.50

Just Accepted

Measurement errors are assumed to be mutually independent across vehicles, topology levels, and update instants. Therefore,

$$\eta_n^{(m)}[\ell] \perp\!\!\!\perp \eta_{n'}^{(m')}[\ell'], \quad (n,m,\ell) \neq (n',m',\ell') \tag{8}$$

To conservatively evaluate the applicability boundary of the low-cost V2X scheme, the following analyses and simulations consistently use conservative delay parameters. Unless otherwise stated, the remaining model parameters follow typical settings in previous CHV studies(Sun et al., 2023; Yang et al., 2026), as listed in **Table 2**.

4 Stability Analysis of Connected Human-Driven Platoons

To analyze the influence of V2X errors on the traffic system, this section derives the linear stochastic dynamics based on the homogeneous CHV platoon model. It then combines the definition of mean-square stability with the linear perturbation boundary to obtain the corresponding stability conditions. Using the measured error distribution parameters from Section 2, the stability boundary of the low-cost V2X platoon under the current error level is further determined.

4.1. Linearized Stochastic Platoon Dynamics

For a homogeneous car-following platoon composed of CHVs, all vehicles ideally stay in an equilibrium state with spacing s_e and velocity v_e. Because V2X introduces the constant bias $\bar{\mu}$, the actual equilibrium spacing shifts to:

$$\tilde{s}_e = s_e + \bar{\mu}\left(\frac{v_e \alpha_n \xi_n}{2\sqrt{ab}\sqrt{1-(v_e/v_0)^4}} \right) \tag{9}$$

Let the vehicle be subject to small perturbations around the equilibrium state, with $\delta s_n(t) = s_n(t) - \tilde{s}_e$ and $\delta v_n(t) = v_n(t) - v_e$. A first-order Taylor expansion of Eq. (1) around the equilibrium point gives the following linear stochastic perturbation equation for $t \in [t_\ell, t_{\ell+1})$:

$$\begin{aligned} \dot{\delta v_n}(t) = {} & f'_{\Delta v} \sum_{m=2}^{M} \beta_m \eta_n^{(m)}[\ell] \\ & + \left(f_v + f_{\Delta v} + f'_{\Delta v} \right) \delta v_n(t-\tau_d) - f_{\Delta v} \delta v_{n-1}(t-\tau_d) \\ & + f_s \delta s_n(t-\tau_d) - f'_{\Delta v} \sum_{m=2}^{M} \beta_m \delta v_{n-m}(t-\tau_d-\tau_c) \end{aligned} \tag{10}$$

where f_v, f_s, $f_{\Delta v}$, and $f'_{\Delta v}$ are the first-order partial derivatives of each variable around the equivalent platoon equilibrium point $(v_e, \tilde{s}_e, 0, 0)$:

$$f_v = -a\left[\frac{4v_e^3}{v_0^4} + \frac{2\tilde{T}(s_0 + \tilde{T}v_e)}{\tilde{s}_e^2} \right] \tag{11}$$

$$f_s = \frac{2a(s_0 + \tilde{T}v_e)^2}{\tilde{s}_e^3} \tag{12}$$

$$f_{\Delta v} = -\sqrt{\frac{a}{b}} \frac{v_e(s_0 + \tilde{T}v_e)}{\tilde{s}_e^2} \tag{13}$$

$$f'_{\Delta v} = -\xi_n \alpha_n \sqrt{\frac{a}{b}} \frac{v_e(s_0 + \tilde{T}v_e)}{\tilde{s}_e^2} \tag{14}$$

where $\tilde{T} = T + (\alpha_n \xi_n \bar{\mu}) / (2\sqrt{ab})$ is the equivalent safe time headway.

To analyze perturbation transfer through the platoon, let $\delta s_n(t) = \hat{s}(t) e^{jkn}$ and $\delta v_n(t) = \hat{v}(t) e^{jkn}$ where j is the imaginary unit and $k \in (0, \pi]$ is the wavenumber(Treiber and Kesting, 2013). A spatial Fourier transform is also applied to the error sequence, and $\hat{\eta}^{(m)}$ denotes the corresponding mode. Combining these expressions with the basic spacing relation $\mathrm{d}s_n / \mathrm{d}t = v_{n-1} - v_n$ gives:

$$\hat{s}(\omega,k) = \frac{e^{-jk}-1}{j\omega} \hat{v}(\omega,k) \tag{15}$$

Substituting the above decomposition into Eq.(10) and applying the temporal Fourier transform gives a single-variable equation for $\hat{v}(\omega,k)$:

$$\mathrm{H}(\omega,k)\hat{v}(\omega,k) = f'_{\Delta v} \sum_{m=2}^{M} \beta_m \hat{\eta}^{(m)}(\omega,k) \tag{16}$$

where $\hat{\eta}^{(m)}(\omega,k)$ is the spatiotemporal frequency-domain representation of the random error at topology level m, and $\mathrm{H}(\omega,k)$ is the characteristic polynomial of the deterministic part:

$$\begin{aligned} \mathrm{H}(\omega,k) = {} & j\omega + f'_{\Delta v} \sum_{m=2}^{M} \beta_m e^{-j\omega(\tau_d+\tau_c)} e^{-jkm} \\ & - \left(f_v + f_{\Delta v} + f'_{\Delta v} + f_s \frac{e^{-jk}-1}{j\omega} - f_{\Delta v} e^{-jk} \right) e^{-j\omega\tau_d} \end{aligned} \tag{17}$$

By the principle of linear superposition, the velocity perturbation can be expressed as the sum of the random error responses from all topology levels: $\hat{v}(\omega,k) = \sum_{m=2}^{M} \frac{f'_{\Delta v}\beta_m}{\mathrm{H}(\omega,k)} \hat{\eta}^{(m)}(\omega,k)$. Therefore, the transfer function from the error at topology level m to the velocity perturbation is:

$$G_{v,m}(\omega,k) = \frac{f'_{\Delta v}\beta_m}{\mathrm{H}(\omega,k)} \tag{18}$$

Combining this result with Eq.(15) gives the transfer function from the error to the spacing perturbation:

$$G_{s,m}(\omega,k) = \frac{e^{-jk}-1}{j\omega} G_{v,m}(\omega,k) \tag{19}$$

Thus, the platoon dynamics can be divided into two parts. $\mathrm{H}(\omega,k)$ characterizes deterministic perturbation propagation, while $G_{v,m}(\omega,k)$ and $G_{s,m}(\omega,k)$ describe the transfer characteristics from the error at each topology level to velocity and spacing perturbations, respectively.

4.2. Mean-Square Stability Conditions

Based on the platoon dynamics, this subsection analyzes stability under stochastic perturbations at two levels. General mean-square stability ensures that the platoon state remains mean-square bounded under finite error input. Strict mean-square stability further requires the bounded perturbation to remain within the effective linearization range at a given confidence level. For a unified notation, $x \in \{v, s\}$ is used below to denote either velocity or spacing. The symbols $\delta x(t)$ and $\delta x_{\max}$ follow this convention and are not defined separately below.

Definition 1 For a homogeneous platoon, if the platoon system state deviation $\delta x(t)$ satisfies the following condition under initial perturbations and finite-intensity stochastic errors:

$$\sup_{t \geq 0} \mathrm{E}\left[\delta x^2(t) \right] \leq c < \infty, \quad \exists\, c \in \mathbb{R}^+ \tag{20}$$

then the platoon is said to be generally mean-square stable.

Theorem 1 If, for any $k \in (0, \pi]$, the characteristic equation of the platoon satisfies two conditions, namely (1) the number of roots with positive real parts is $N = 0$, and (2) the real-part equation $\mathrm{R}(\omega,k) = 0$ and the imaginary-part equation $\mathrm{I}(\omega,k) = 0$ have no common real root, then the homogeneous CHV platoon is generally mean-square stable.

In the above conditions, N is calculated using Eq. (21). In Eq. (21), d is the system dimension and equals 2 in this paper. $\rho_1^{\mathrm{R}} \geq \cdots \geq \rho_{N_{\mathrm{R}}}^{\mathrm{R}} > 0$ and $\rho_1^{\mathrm{I}} \geq \cdots \geq \rho_{N_{\mathrm{I}}}^{\mathrm{I}} = 0$ are the positive real zeros of $\mathrm{R}(\omega,k)$ and the nonnegative real zeros of $\mathrm{I}(\omega,k)$, respectively. $\mathrm{sgn}(\cdot)$ denotes the sign function.

Proof As shown in Section 3, the error has finite variance σ_η^2. According to linear time-invariant stochastic response theory(Papoulis and Pillai, 2002) and Parseval's identity, there exists a finite positive constant C_η, determined by σ_η^2 and the error update characteristics, such that:

Just Accepted

$$N=\begin{cases} p+(-1)^{p}\sum_{\nu=1}^{N_{\mathrm{R}}}(-1)^{\nu+1}\operatorname{sgn}\mathrm{I}\left(\rho_{\nu}^{\mathrm{R}},k\right) & \text{if } d=2p \\ p+\dfrac{1}{2}+(-1)^{p}\left[\dfrac{1}{2}(-1)^{N_1}\operatorname{sgn}\mathrm{R}\left(0,k\right)+\sum_{\nu=1}^{N_1-1}(-1)^{\nu}\operatorname{sgn}\mathrm{R}\left(\rho_{\nu}^{\mathrm{I}},k\right)\right] & \text{if } d=2p+1 \end{cases} \tag{21}$$

$$\begin{aligned}\mathrm{R}\left(\omega,k\right)=&-\omega^{2}+f_{s}\left(\cos(\omega\tau_{d})-\cos(\omega\tau_{d}+k)\right)\\&-\omega\left[\begin{array}{l}f_{v}\sin(\omega\tau_{d})+f_{\Delta v}\left(\sin(\omega\tau_{d})-\sin(\omega\tau_{d}+k)\right)\\+f_{\Delta v}^{'}\left(\sin(\omega\tau_{d})-\sum_{m=2}^{M}\beta_{m}\sin(\omega\tau_{d}+\omega\tau_{c}+km)\right)\end{array}\right]=0\end{aligned} \tag{22}$$

$$\begin{aligned}\mathrm{I}\left(\omega,k\right)=&-f_{s}\left(\sin(\omega\tau_{d})-\sin(\omega\tau_{d}+k)\right)\\&-\omega\left[\begin{array}{l}f_{v}\cos(\omega\tau_{d})+f_{\Delta v}\left(\cos(\omega\tau_{d})-\cos(\omega\tau_{d}+k)\right)\\+f_{\Delta v}^{'}\left(\cos(\omega\tau_{d})-\sum_{m=2}^{M}\beta_{m}\cos(\omega\tau_{d}+\omega\tau_{c}+km)\right)\end{array}\right]=0\end{aligned} \tag{23}$$

$$\sup_{t\geq 0}\mathrm{E}\left[\delta x^{2}(t)\right]\leq C_{\eta}\sup_{k\in(0,\pi]}\sum_{m=2}^{M}\int_{-\infty}^{+\infty}\left|G_{x,m}(\omega,k)\right|^{2}\mathrm{d}\omega \tag{24}$$

Inspection of Eqs.(18) and (19) shows that the poles of $G_{x,m}(\omega,k)$ are determined by the characteristic equation $\mathrm{H}(\omega,k)=0$. If all characteristic roots lie strictly in the left half of the complex plane for every $k\in(0,\pi]$, the frequency-domain integral above converges. A constant $c\in\square^{+}$ therefore exists such that Definition 1 holds.

Following Yang et al. (2026), Euler's formula is used to separate the real and imaginary parts of $\mathrm{H}(\omega,k)=0$, giving Eq. (22) and Eq. (23). According to Eq. (21), the system has no characteristic roots in the right half-plane if and only if $N=0$ (Erman et al., 2018). In addition, if Eq. (22) and Eq. (23) have no common real root, the system has no characteristic roots on the imaginary axis. Together, these two conditions ensure that all characteristic roots lie in the left half of the complex plane. This proves the theorem.

General mean-square stability guarantees that system perturbations are bounded. To ensure the validity of the linearized system constructed in Eq. (10), the probability that the steady-state perturbation exceeds the effective linear boundary must be further constrained.

Lemma 1 The effective linear boundary $\delta x_{\max}$ of $\delta x(t)$ is:

$$\delta x_{\max}=\frac{2\grave{o}\left|f_{x}\right|}{f_{x,\max}^{(2)}} \tag{25}$$

where $\grave{o}\square 1$ is a small tolerance factor, taken as 0.1 in this paper. f_x is the first-order partial derivative in the x direction, and $f_{x,\max}^{(2)}$ is the maximum absolute value among the second-order partial derivatives obtained by differentiating f_x with respect to the state variables again.

Proof The second-order Taylor remainder of Eq. (10) is required to be bounded by $\grave{o}$ times the first-order term, namely $\left|\frac{1}{2}f_{x,\max}^{(2)}(\delta x)^{2}\right|\leq\grave{o}\left|f_{x}\delta x\right|$. Simplifying this inequality proves the lemma.

Definition 2 Under general mean-square stability, after the system reaches steady state, if $\delta x[\ell]=\delta x(t_{\ell})$ satisfies the following condition at any update instant with confidence level $1-\gamma$, where γ is the tail truncation probability and is commonly taken as 3‰:

$$\mathrm{P}\left(\left|\delta x[\ell]\right|\leqslant\delta x_{\max}\right)\geq 1-\gamma \tag{26}$$

then the platoon is said to have strict mean-square stability.

Theorem 2 If a homogeneous CHV platoon has general mean-square stability and its V2X errors follow an LMM-3 distribution, then a sufficient condition for strict mean-square stability of the steady-state perturbation $\delta x[\ell]$ at update instant t_{ℓ} is:

$$\frac{2}{\pi}\int_{0}^{\infty}\frac{\sin\left(u\delta x_{\max}\right)}{u}\mathrm{Re}\left[\varphi_{x}(u)\right]\mathrm{d}u\geq 1-\gamma \tag{27}$$

where $\varphi_{x}(u)$ is the characteristic function of the steady-state perturbation $\delta x[\ell]$:

$$\varphi_{x}(u)=\prod_{m=2}^{M}\prod_{z\in\square}\prod_{r=1}^{\infty}\left[\sum_{i=1}^{3}\pi_{i}\frac{\exp\left[juh_{x,m}[z,r](\mu_{i}-\bar{\mu})\right]}{1+\lambda_{i}^{2}h_{x,m}^{2}[z,r]u^{2}}\right] \tag{28}$$

Here, $h_{x,m}[z,r]$ denotes the response coefficient from the error at topology level m, relative position z, and a lag of r update periods to state x. In the subsequent numerical calculations, the infinite product above is truncated using a threshold of 10^{-4}.

Proof Applying the inverse transform to the frequency-domain transfer function $G_{x,m}(\omega,k)$ in vehicle space and time gives the spatiotemporal impulse response at topology level m:

$$g_{x,m}(z,\tau)=\frac{1}{(2\pi)^{2}}\int_{-\pi}^{\pi}\int_{-\infty}^{+\infty}G_{x,m}(\omega,k)e^{j(kz+\omega\tau)}\,\mathrm{d}\omega\mathrm{d}k \tag{29}$$

where z is the difference between the vehicle indices at the error input and state response positions, and τ is the time lag between the error occurrence and the current state response.

Integrating over the r th update period $[t_{\ell-r},t_{\ell-r+1})$ gives the response coefficient of the corresponding error sample to the current state:

$$h_{x,m}[z,r]=\int_{(r-1)\Delta t_{e}}^{r\Delta t_{e}}g_{x,m}(z,\tau)\mathrm{d}\tau,\quad r\in\square^{+} \tag{30}$$

At steady state, the state perturbation can be expressed as the linear superposition of random error responses over all topology levels, relative vehicle positions, and historical update periods:

$$\delta x[\ell]=\sum_{m=2}^{M}\sum_{z\in\square}\sum_{r=1}^{\infty}h_{x,m}[z,r]\eta_{z,r}^{(m)} \tag{31}$$

where $\eta_{z,r}^{(m)}$ is the V2X random error sample at topology level m, relative vehicle position z, and a lag of r update periods.

Because the characteristic function of a sum of independent random variables equals the product of their characteristic functions, substituting the LMM-3 error characteristic function $\varphi_{\eta}(u)=\sum_{i=1}^{3}\pi_{i}\frac{e^{ju(\mu_{i}-\bar{\mu})}}{1+\lambda_{i}^{2}u^{2}}$ gives:

$$\varphi_{x}(u)=\prod_{m=2}^{M}\prod_{z\in\square}\prod_{r=1}^{\infty}\left[\sum_{i=1}^{3}\pi_{i}\frac{\exp\left[juh_{x,m}[z,r](\mu_{i}-\bar{\mu})\right]}{1+\lambda_{i}^{2}h_{x,m}^{2}[z,r]u^{2}}\right] \tag{32}$$

Finally, the characteristic function inversion formula gives the probability that $\delta x[\ell]$ lies within the effective linear interval:

$$\mathrm{P}\left(\left|\delta x[\ell]\right|\leqslant\delta x_{\max}\right)=\frac{2}{\pi}\int_{0}^{\infty}\frac{\sin(u\delta x_{\max})}{u}\mathrm{Re}\left[\varphi_{x}(u)\right]\mathrm{d}u \tag{33}$$

When this probability is no less than $1-\gamma$, the platoon has strict mean-square stability. This proves the theorem.

Just Accepted

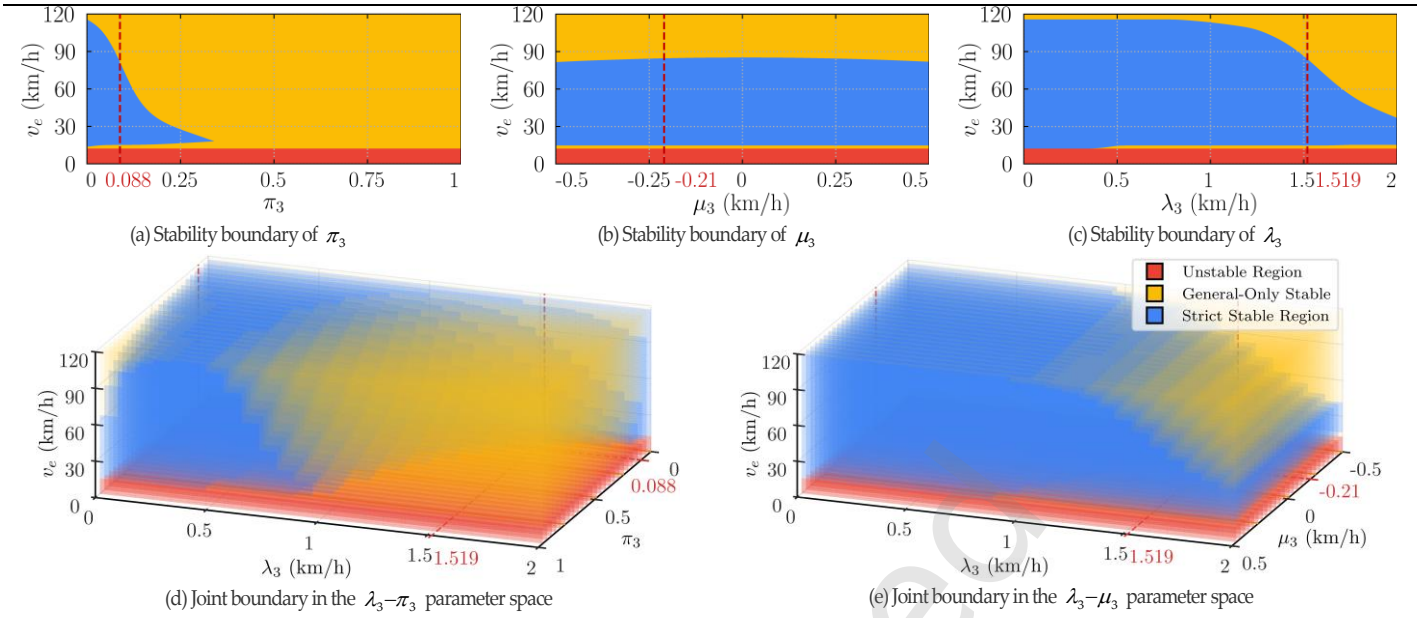

Fig. 2. Variation Trends of Mean-Square Stability

4.3. Stability Boundaries under V2X Errors

This subsection applies the Overall group error distribution parameters from Section 2 and the parameters in **Table 2** to the platoon system using the mean-square stability conditions derived above. The effects of the LMM-3 tail component parameters on the platoon stability boundary are examined by varying π_3, μ_3, and λ_3 separately. The results are shown in **Fig. 2(a)** to **(c)**.

Overall, the unstable region is mainly concentrated in the low-speed range, while the platoon has good general mean-square stability over common driving speeds. The three parameters, however, have clearly different effects on strict mean-square stability. As π_3 increases, the strict mean-square stable region contracts substantially. When $\pi_3 > 0.3$, this region disappears completely. In comparison, the stability boundary is less sensitive to μ_3 and contracts only slightly as μ_3 increases. For λ_3, the boundary changes gradually when $\lambda_3 \le 1.2$ km/h, but contracts much faster when $\lambda_3 > 1.2$ km/h. Thus, π_3 and λ_3 are the main factors affecting the stability boundary, whereas μ_3 has a relatively limited effect. The red dashed lines indicate the measured parameters of the Overall group. They remain within the strict mean-square stable region over a wide range of operating speeds, showing that the current measured error level has not crossed the main stability boundary.

To further consider joint changes in tail parameters, **Fig. 2(d)** and **(e)** show the stability distributions in the $\lambda_3 - \pi_3$ and $\lambda_3 - \mu_3$ parameter spaces, respectively. **Fig. 2(d)** shows that π_3 and λ_3 jointly affect the strict stability region, and an increase in either parameter reduces the feasible operating speed range. A smaller π_3 can increase the system's tolerance of a larger λ_3 to some extent. In **Fig. 2(e)**, the stability boundary changes little along the μ_3 direction but changes more substantially along the λ_3 direction, consistent with the single-parameter results. Overall, the current measured tail parameters retain a certain stability margin, but this margin is mainly limited by the occurrence probability and scale of heavy-tailed errors. The analytical stability results therefore support the feasibility of low-cost V2X within the parameter range studied.

The above analysis is based on a linear stochastic system near the equilibrium state and is mainly used to determine the applicability boundary in terms of stability within the error parameter space. The next section presents Monte Carlo simulations to further examine the effects of nonlinear vehicle responses, transient perturbation propagation, and random error realizations on actual platoon operation.

5 Monte Carlo Simulations under Different Error Regimes

To further evaluate the traffic benefits of the low-cost V2X scheme, this section conducts Monte Carlo simulations and defines three error regimes based on the LMM-3 components. Regime 1 consists of the dominant Components 1 and 2 and represents nominal small errors. Regime 2 retains only the low-probability, large-magnitude Component 3 and serves as a stress test under persistent tail errors. Regime 3 uses all three components and their measured mixing proportions and represents the actual smartphone error level. In addition, a CHV platoon without measurement errors and a human-driven vehicle (HDV) platoon governed by the IDM are used as baselines. They quantify the performance loss caused by measured errors relative to ideal V2X conditions and the stability benefit of low-cost V2X relative to conventional vehicles, respectively.

5.1. Simulation Setup

As shown in **Fig. 3**, the simulated platoon contains 51 vehicles, including one lead vehicle and 50 follower vehicles. All vehicle parameters are taken from **Table 2**. At the initial time $t = 0$, all vehicles have a velocity of $v_e = 15$ m/s, and their initial spacing is the equivalent equilibrium spacing corresponding to this velocity. The first 10 vehicles form the leading platoon, whose errors follow the empirical full mixture distribution of the Overall group. The remaining $N_E = 41$ vehicles form the experimental platoon, and the corresponding error inputs are applied according to each error regime. Each experiment is repeated 10^4 times to calculate the median velocity and spacing responses, as well as the minimum to maximum, 0.15% to 99.85%, and 5% to 95% percentile intervals. The lead-vehicle perturbation is set as:

$$v_0(t) = \begin{cases} v_e, & \text{if } 0 \le t < 10 \\ v_e - 1.5(t-10), & \text{if } 10 \le t < 15 \\ v_e + 1.5(t-20), & \text{if } 15 \le t < 20 \\ v_e, & \text{if } 20 \le t \le T_E \end{cases} \tag{34}$$

Just Accepted

The total simulation time is $T_E = 150\,\mathrm{s}$, and the time step is $\Delta t = 0.01\,\mathrm{s}$. The velocity and spacing of follower vehicles are updated according to:

$$v_n(t+\Delta t) = \max\left(v_n(t) + a_n(t)\Delta t, 0\right) \tag{35}$$

$$s_n(t+\Delta t) = \max\left(s_n(t) + \left(v_{n-1}(t) - v_n(t)\right)\Delta t, 0\right) \tag{36}$$

To quantify the stability of the experimental platoon, the velocity standard deviation R_{SD} and mean absolute deviation R_{MAD} are introduced. Larger values of R_{SD} and R_{MAD} indicate weaker platoon stability. The metrics are defined as follows:

$$R_{\mathrm{SD}} = \sqrt{\frac{1}{T_E}\frac{1}{N_E - 1}\sum_{t=0}^{T_E}\sum_{n=10}^{50}\left(v_n(t) - v_e\right)^2 \Delta t} \tag{37}$$

$$R_{\mathrm{MAD}} = \frac{1}{T_E}\frac{1}{N_E}\sum_{t=0}^{T_E}\sum_{n=10}^{50}\left|v_n(t) - v_e\right|\Delta t \tag{38}$$

5.2. Simulation Results

The simulation results for the three error regimes and two baseline groups are shown in **large tail** errors mainly intensify fluctuations and reduce the stability margin

Table 3. The perturbation propagation processes for the three error regimes and the HDV group are further shown in **Fig. 4**. Overall, R_{SD} and R_{MAD} are substantially lower in all three V2X error regimes than in the HDV baseline. Their average improvements relative to the HDV baseline all exceed 74%, indicating that V2X state sharing can effectively suppress platoon velocity fluctuations under different smartphone measurement errors.

Specifically, as shown in the first and third columns of **Fig. 4**, the lead-vehicle perturbation in Regime 1 gradually decays as it propagates downstream, and the median velocity and spacing trajectories return rapidly to the equilibrium state. The overall response in Regime 3 is close to that in Regime 1, with only a slight widening of the deviation intervals. The corresponding R_{SD} and R_{MAD} values are 1.081 and 0.360, respectively, which are close to the Regime 1 values of 1.077 and 0.358. Their average performance degradations relative to the Ideal CHV are only 1.32% and 1.79%, respectively. This indicates that, under the measured mixing proportions, the dominant small-magnitude errors determine the main platoon response, while the low-probability tail errors do not substantially reduce the overall stability benefit.

In contrast, as shown in the second column of **Fig. 4**, Regime 2 produces stronger velocity oscillations and wider velocity and spacing deviation intervals. A clear band of downstream perturbation propagation forms at approximately 50-100s. Its R_{SD} and R_{MAD} increase to 1.127 and 0.381, respectively, and its average performance degradation relative to the Ideal CHV reaches 6.93%, clearly exceeding those of the other two error regimes. Because this regime continuously applies the low-probability tail component of the measured distribution, its results mainly represent a stress test under persistent heavy-tailed errors. Although the stability margin decreases, the median velocity and spacing trajectories still return to the equilibrium state after the perturbation. The average improvement relative to the HDV baseline remains 74.66%. Thus, large tail errors mainly intensify fluctuations and reduce the stability margin without destroying the overall mean-square boundedness of the platoon.

Table 3. Quantitative Comparison across Regimes

Case	R_{SD}	R_{MAD}	Avg. Impr.	Avg. Degr.
Ideal CHV	1.064	0.353	76.25%	–
Regime 1	1.077	0.358	75.95%	1.32%
Regime 2	1.127	0.381	74.66%	6.93%
Regime 3	1.081	0.360	75.84%	1.79%
HDV	3.713	1.874	–	–

Note: R_{SD} and R_{MAD} are averaged over 10^4 Monte Carlo runs; Avg. Impr. and Avg. Degr. are the mean relative changes of both metrics relative to the HDV and Ideal CHV baselines, respectively.

The HDV group shows clearly different perturbation propagation characteristics. As shown in the fourth column of **Fig. 4**, velocity oscillations and spacing compression and expansion waves continuously amplify along the platoon under the same lead-vehicle perturbation, causing local emergency stops. None of the three V2X error regimes shows similar persistent amplification. In particular, Regime 3, which represents the actual smartphone error level, achieves an average improvement of 75.84% relative to the HDV baseline and degrades by only 1.79% relative to the Ideal CHV. This shows that the performance loss caused by current measured smartphone errors is much smaller than the stability benefit of V2X state sharing. It also confirms that low-probability, large-magnitude heavy-tailed errors are the main risk limiting the stability margin of low-cost V2X. At the current smartphone perception accuracy, low-cost V2X can therefore retain most of the cooperative benefit of ideal V2X at the platoon level. Future deployment should focus on suppressing tail errors and evaluating how changes in the HDV proportion in mixed traffic affect system stability benefits.

6 Conclusion

This paper evaluated the applicability boundary and application potential of smartphones as low-cost transitional V2X terminals from a platoon perspective. Based on real-vehicle data, the statistical characteristics of smartphone-based vehicle state perception errors were characterized. Mean-square stability analysis and Monte Carlo simulations were then combined to evaluate their influence on disturbance propagation in CHV platoons from both analytical and numerical perspectives. The main findings are as follows:

1) Smartphone-based vehicle state perception errors can be effectively represented by a three-component Laplace mixture distribution. Across different aggregation dimensions, their structure shows a similar mixture form. It consists of two high-proportion, small-magnitude main components with opposite directions and one low-probability, large-magnitude tail component. Differences among vendors and device generations are mainly reflected in tail characteristics. Recent devices reduce the probability of abnormal large errors, but they cannot fully eliminate heavy tails.

Just Accepted

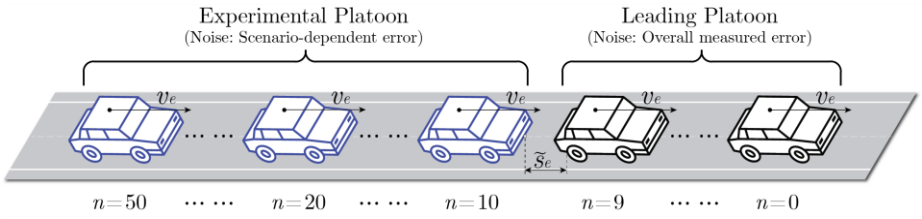

Fig. 3. Schematic Illustration of the Numerical Experiments
(Vehicles indexed as $n = 10,20,30,\ldots$ are highlighted using distinctive colors in the subsequent analyses.)

2) Mean-square stability analysis based on the measured LMM-3 error distribution shows that the current smartphone error level retains a good stability margin over common driving speeds. The occurrence probability and scale parameter of the heavy-tailed component are the main factors affecting the strict mean-square stability boundary, whereas the location parameter has a relatively limited effect. Joint parameter analysis further shows that a lower occurrence probability of heavy-tailed errors can increase the system's tolerance of a larger tail scale to some extent. These results analytically define the applicability boundary of low-cost V2X under heavy-tailed measurement errors and show that suppressing low-probability, large-magnitude errors is critical to expanding its feasible range.

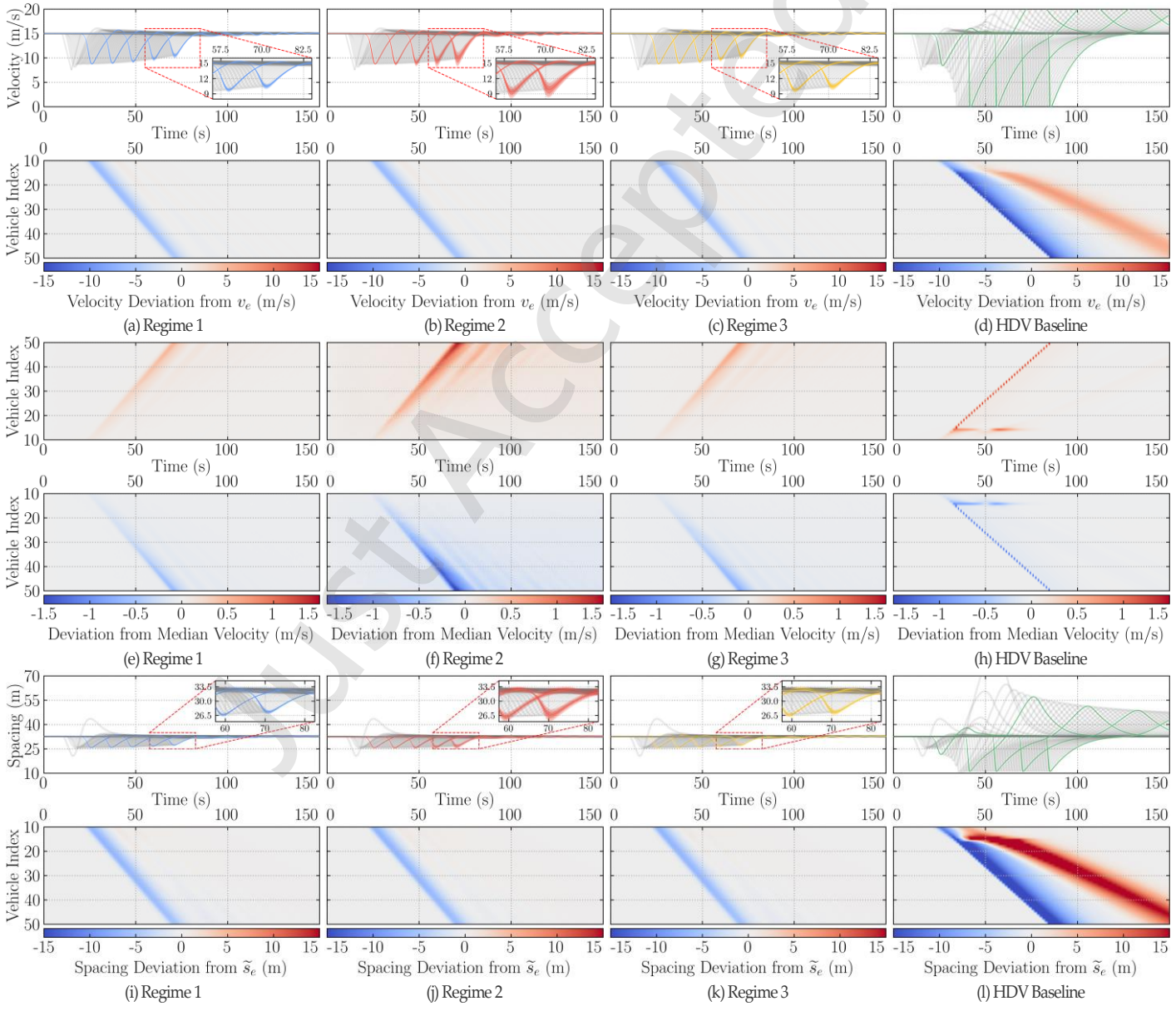

Just Accepted

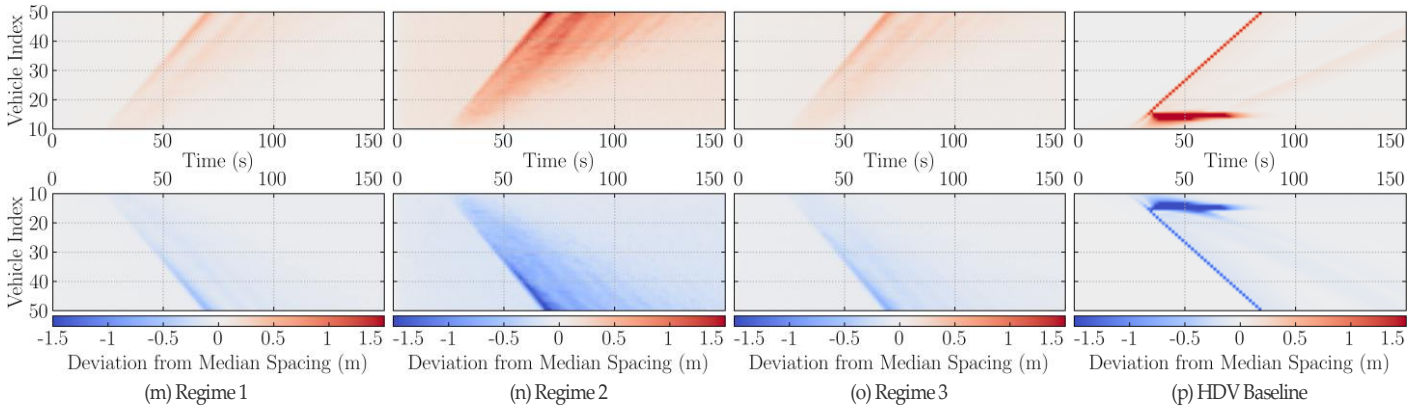

Fig. 4. Monte Carlo Responses under Different Error Regimes (From top to bottom, the rows show velocity trajectories, velocity deviations from the median, spacing trajectories, and spacing deviations from the median.)

3) The Monte Carlo simulations further quantify the platoon stability benefits under different error regimes. The empirical full mixture regime achieves an average improvement in platoon stability performance of 75.84% relative to the HDV baseline, while its average performance degradation relative to the Ideal CHV is only 1.79%. Even in the stress test with persistent errors from the tail component, the average improvement relative to the HDV baseline remains 74.66%, although the performance degradation relative to the Ideal CHV increases to 6.93%. These results show that the performance loss caused by current measured smartphone errors is substantially smaller than the stability benefit of V2X state sharing. They also confirm that low-probability heavy-tailed errors are the main risk limiting the stability margin.

These results also provide guidance for the design, performance evaluation, and application validation of low-cost connected terminals. Terminal error evaluation should consider not only the mean error or overall fluctuation level but also the occurrence probability and scale of heavy-tailed errors or corresponding high-percentile exceedance indicators. Terminal algorithms should prioritize the detection and suppression of abnormal large errors and may combine multisource information, such as IMU measurements, to improve the robustness of state perception. For practical applications, system benefits can first be further validated in noncritical safety scenarios, including traffic efficiency improvement and beyond-line-of-sight information assistance.

Overall, smartphones at their current perception accuracy have shown potential as low-cost V2X terminals at the platoon level, but substantial gaps remain before practical engineering application. Future research will extend the platoon-level feasibility analysis to system implementation at the microscopic vehicle level, develop a low-cost V2X system architecture for practical applications, and further consider the temporal correlation of smartphone GNSS errors, possible spatiotemporal error correlations among vehicles, and engineering factors such as communication. Future real-vehicle control experiments will examine the effects of these factors on system performance and extend the study to mixed traffic and complex operating environments involving lane changing, diverging, and merging.

Appendix A

This appendix provides supplementary information on the field experiments. As shown in **Fig. 1**, six smartphones were mounted on the same bracket near the upper central area inside the windshield for synchronous data acquisition. Reference data were collected by a laptop connected simultaneously to the roof-mounted UM982 RTK-GNSS receiver and the in-vehicle OBD-II interface. **Table 4** summarizes the device information, operating systems, main recorded data, and sampling rates for all data sources. The complete raw experimental dataset is publicly available at https://huggingface.co/datasets/InterestingITS/smartphone_in_vehicle_multisensor.

Appendix B

This appendix provides further details of data processing and error distribution fitting. **Table 5** summarizes the data filtering results, final effective samples, and time correction ranges under different aggregation dimensions. Based on these effective samples, this paper refers to existing GNSS error modeling studies(Teunissen, 2020; Duong et al., 2021; Specht, 2021; Yan et al., 2025). Gaussian, Logistic, Laplace, constrained Student's t distribution (C-t Dist, $\nu \geq 3$), Gaussian Mixture Model (GMM), Laplace Mixture Model (LMM), and Contaminated Normal (CN) were selected as candidate models. The number of mixture components was limited to 2 and 3 to balance fitting capability and model complexity.

The parameters of all candidate models were calibrated by maximum likelihood estimation. Model evaluation used three types of indicators: Bayesian information criterion (BIC), Anderson–Darling (AD) statistic, and high-percentile error deviation. BIC measures the overall fitting performance while considering model complexity. AD evaluates the model's ability to characterize the distribution tail. ΔP_{95} and ΔP_{99} denote the absolute deviations between the model-estimated 95% and 99% percentiles and the empirical percentiles, respectively. Smaller values indicate better fitting performance. The evaluation results of different models under each dimension are shown in **Table 6**.

Table 6 shows that LMM-3 obtains the lowest or second-lowest BIC value in most dimensions and the smallest AD value in all dimensions. This indicates that it is more stable in both overall fitting and tail characterization. Although a few models perform slightly better for some percentile deviations, LMM-3 provides the best overall balance. Therefore, this paper uses LMM-3 to describe smartphone-based V2X speed errors and adopts it as the error input model for subsequent stochastic platoon stability analysis.

Just Accepted

Table 4. Overview of Experimental Data Sources and Recorded Information

Data Source	Device	OS	Recorded Data and Sampling Rate
Apple	iPhone 15 Pro Max	iOS 26.3.1 / 26.5	Motion/Attitude (100 Hz); GNSS (1 Hz); Device Status (1 Hz)
	iPhone 8 Plus	iOS 16.7.15	Motion/Attitude (100 Hz); GNSS (1 Hz); Device Status (1 Hz)
Samsung	Galaxy Z Fold5	Android 16	Motion/Attitude (100–500 Hz); GNSS (0.1–1 Hz); Device Status (1–25 Hz)
	Galaxy S10	Android 11	Motion/Attitude (100–400 Hz); GNSS (0.1–1 Hz); Device Status (1–25 Hz)
Xiaomi	Mi 15	Android 16	Motion/Attitude (100–500 Hz); GNSS (0.3–1 Hz); Device Status (1–25 Hz)
	Mi 11	Android 13	Motion/Attitude (100–400 Hz); GNSS (0.3–1 Hz); Device Status (1–25 Hz)
RTK-GNSS	UM982	–	RTK Results (20 Hz); Raw Data (1–20 Hz); Trajectory Data; RTCM Data
OBD-II	ELM327	–	Vehicle Speed (5–9 Hz)

Table 5. Supplementary Information on Field Experiment and Effective Samples

Dimension	Category	Raw Samples	Hard Excl.	Dyn. Excl.	Eff. Samples	Eff. Ratio (%)	Time Shift (s)
Scenario	Highway	101921	105	48135	53681	52.67	[0.00, 0.00]
	Expressway	90417	56	35005	55356	61.22	[-0.64, 0.10]
	Urban Road	132284	697	70199	61388	46.41	[-0.77, 0.50]
Vehicle	VW Golf	191653	686	92192	98775	51.54	[-0.76, 0.50]
	VW Passat	132969	172	61147	71650	53.88	[-0.77, 0.44]
Vendor	Apple	108211	586	50774	56851	52.54	[-0.48, 0.00]
	Samsung	108213	150	51262	56801	52.49	[-0.20, 0.08]
	Xiaomi	108198	122	51303	56773	52.47	[-0.77, 0.50]
Generation	Recent	162340	232	76932	85176	52.47	[-0.48, 0.50]
	Earlier	162282	626	76407	85249	52.53	[-0.77, 0.00]
Overall	All Data	324622	858	153339	170425	52.50	[-0.77, 0.50]

Note: Excl., Dyn., and Eff. denote exclusion, dynamic exclusion, and effective, respectively. Time shift is reported as [min, max].

Just Accepted

Table 6. Performance Comparison of Fitting Models under Different Aggregation Dimensions

Dimension	Category	Metric	Gaussian	Logistic	Laplace	C-t Dist	GMM-2	GMM-3	LMM-2	LMM-3	CN
Scenario	Highway	BIC	104029	80752	73612	70435	72174	70326	69456	**69349**	72182
		AD	2379.591	519.485	137.963	54.616	62.237	29.085	6.145	**1.210**	64.436
		ΔP_{95}	0.255	0.008	0.054	0.062	0.030	0.017	0.007	0.006	**0.005**
		ΔP_{99}	0.207	0.442	0.255	0.286	0.446	0.199	0.033	**0.020**	0.528
	Expressway	BIC	161875	120671	111625	105589	109107	105280	104558	**104421**	109088
		AD	4054.561	708.341	235.419	65.965	121.118	46.830	7.070	**2.752**	110.533
		ΔP_{95}	0.671	0.048	0.109	0.092	0.065	0.060	**0.006**	0.008	0.062
		ΔP_{99}	0.112	0.830	0.574	0.695	1.361	0.103	0.102	**0.069**	1.323
	Urban Road	BIC	138085	103846	94643	88747	90443	87470	87513	**87193**	90502
		AD	3618.589	744.374	262.846	81.443	85.426	5.971	16.823	**2.387**	78.698
		ΔP_{95}	0.419	0.083	0.141	0.010	0.054	0.013	0.024	**0.004**	0.030
		ΔP_{99}	0.033	0.393	0.178	0.260	0.593	0.155	**0.029**	0.110	0.954
Vehicle	VW Golf	BIC	223779	174206	159227	151401	154144	150240	149030	**148688**	153994
		AD	5305.237	1179.493	371.981	125.559	162.954	51.980	15.470	**2.330**	117.549
		ΔP_{95}	0.348	0.023	0.076	0.075	0.088	0.048	0.008	0.016	**0.005**
		ΔP_{99}	0.266	0.599	0.387	0.461	0.518	0.146	**0.051**	0.064	0.666
	VW Passat	BIC	191347	135186	123707	115647	120738	115715	114382	**114196**	120735
		AD	5424.740	885.400	296.454	82.389	161.192	68.609	8.950	**4.661**	164.580
		ΔP_{95}	0.624	0.065	0.124	0.050	0.045	0.068	**0.011**	0.011	0.034
		ΔP_{99}	0.069	0.584	0.356	0.459	1.257	0.134	**0.011**	0.046	1.355
Vendor	**Apple** iPhone 15PM (2023) iPhone 8P (2017)	BIC	167780	143823	135044	131629	132180	132048	129698	**129534**	132134
		AD	2750.378	722.838	232.314	108.977	77.356	57.294	7.056	**0.906**	65.342
		ΔP_{95}	65.342	0.060	0.142	0.077	0.085	**0.007**	0.010	0.008	0.148
		ΔP_{99}	0.474	0.852	0.539	0.641	0.508	0.384	**0.052**	0.118	0.747
	Samsung Galaxy Fold5 (2023) Galaxy S10 (2019)	BIC	131259	58747	50900	**41364**	46986	41543	41714	41432	46938
		AD	6488.357	537.697	196.184	12.463	130.150	14.013	18.898	**5.856**	153.453
		ΔP_{95}	0.710	0.062	0.105	0.007	0.019	0.012	0.029	**0.005**	0.021
		ΔP_{99}	0.580	0.243	0.085	0.149	1.597	**0.052**	0.073	0.082	1.369
	Xiaomi Mi 15 (2024) Mi 11 (2021)	BIC	99278	84462	80831	**79112**	80884	79643	79632	79122	80360
		AD	1254.608	216.806	38.543	5.629	19.171	9.787	26.022	**1.851**	28.735
		ΔP_{95}	0.144	0.002	0.059	0.014	0.061	0.008	0.029	**0.001**	0.019
		ΔP_{99}	0.210	0.295	0.087	0.029	0.215	0.120	0.021	**0.005**	0.318
Generation	**Recent** iPhone 15PM (2023) Galaxy Fold5 (2023) Mi 15 (2024)	BIC	186178	135651	127609	**121755**	127298	122488	122155	121773	127153
		AD	4115.756	495.173	116.195	16.897	181.894	11.021	21.081	**2.841**	135.374
		ΔP_{95}	0.365	0.020	0.077	0.026	0.056	**0.002**	0.020	0.004	0.047
		ΔP_{99}	**0.004**	0.362	0.150	0.143	0.643	0.007	0.054	0.046	0.840
	Earlier iPhone 8P (2017) Galaxy S10 (2019) Mi 11 (2021)	BIC	227432	172073	154364	145212	147348	141322	140247	**140052**	147241
		AD	6374.208	1643.275	640.792	264.750	180.951	42.265	8.961	**4.319**	150.381
		ΔP_{95}	0.544	0.050	0.103	0.113	0.056	**0.011**	0.021	0.028	0.150
		ΔP_{99}	0.249	0.807	0.585	0.760	0.816	**0.094**	0.198	0.269	0.954
Overall	All Data	BIC	418562	309551	283050	267090	276012	265665	263512	**263029**	275774
		AD	10891.084	2065.620	666.648	207.824	375.759	89.539	22.281	**5.444**	290.658
		ΔP_{95}	0.471	0.041	0.096	0.064	0.074	0.044	**0.001**	0.018	0.026
		ΔP_{99}	0.114	0.592	0.373	0.459	0.835	0.121	**0.031**	0.103	0.987

Note: ΔP_{95} and ΔP_{99} represent the absolute deviations between the model-estimated theoretical percentiles and the empirical percentiles. Abbreviations: C-t Dist (Constrained Student's t-distribution with $\nu \geq 3$), GMM (Gaussian Mixture Model), LMM (Laplace Mixture Model), CN (Contaminated Normal).

Just Accepted

Author contributions

Baofeng Sun: Writing – review & editing, Supervision, Validation, Funding acquisition. **Wenyu Yang:** Writing – original draft, Writing – review & editing, Software, Methodology, Formal analysis, Data curation, Conceptualization. **Guodong Ma:** Writing – review & editing, Methodology, Data curation, Project administration. **Xiaoxiang Na:** Methodology, Validation.

Replication and data sharing

The complete raw experimental dataset is publicly available on Hugging Face at https://huggingface.co/datasets/InterestingITS/smartphone_in_vehicle_multisensor. The source codes and replication package are available on ETS Data at https://doi.org/10.26599/ETSD.2026.9190093.

Acknowledgements

This research was supported by National Natural Science Foundation of China (grant number 52472313). The authors gratefully acknowledge Huxing Zhou, Yuqi Chen, and Qibo Liu for providing support and resources for the experimental work.

Declaration of competing interest

The authors have no competing interests to declare that are relevant to the content of this article.

Declaration of generative AI and AI-assisted technologies in the writing process

During the preparation of this work, the authors used ChatGPT for language polishing. After utilizing this tool, the authors thoroughly reviewed and edited the content as necessary and take full responsibility for the final content of the published article.

Just Accepted

References

Abdel-Aty, M.A., Cai, Q., Agarwal, S., Islam, Z., Li, P., Zhang, S., et al., 2020. Using smartphone as on-board unit (OBU) emulator implementation study. Florida Department of Transportation Report BDV24-977-30.

Arena, F., Pau, G., Severino, A., 2019. V2X communications applied to safety of pedestrians and vehicles. J Sens Actuator Netw, 9, 3.

Bouadi, M., Jia, B., Jiang, R., Li, X., Gao, Z.-Y., 2022. Stochastic factors and string stability of traffic flow: Analytical investigation and numerical study based on car-following models. Transport Res B-Meth, 165, 96–122.

China Government Procurement Network, 2026. Award results announcement for phase II of the C-V2X retrofit project for innovative applications of vehicle-road-cloud integrated intelligent connected vehicles. https://www.ccgp.gov.cn/cggg/dfgg/zbgg/202601/t20260131_26138414.htm

Cui, S., Yu, B., 2025. Impact of CAV performance degradation and cooperative prompting on the stability and fundamental diagram of mixed traffic flow. China J Highw Transp, 38, 16–29.

Dong, J., Wang, J., Luo, D., 2022. Impact of connected and autonomous vehicles on traffic safety of mixed traffic flow: From the perspective of connectivity and spatial distribution. Transport Saf Environ, 4, tdac021.

Duong, V., Harima, K., Choy, S., Rizos, C., 2021. GNSS best integer equivariant estimation using multivariant t-distribution: A case study for precise point positioning. J Geod, 95, 10.

Erman, S., Sevindir, H.K., Demir, A., 2018. The stability analysis of a system with two delays. Bound Value Probl, 2018, 106.

Fei, R., Yang, L., Hei, X., Hu, B., Li, A., 2023. A car-following model based on the optimized velocity and its security analysis. Transport Saf Environ, 5, tdac077.

Ge, J.I., Avedisov, S.S., He, C.R., Qin, W.B., Sadeghpour, M., Orosz, G., 2018. Experimental validation of connected automated vehicle design among human-driven vehicles. Transport Res C-Emer, 91, 335–352.

Gu, X., Duan, W., Zhang, G., Hou, J., Peng, L., Wen, M., et al., 2026. Digital twin technology for intelligent vehicles and transportation systems: A survey on applications, challenges and future directions. IEEE Commun Surv Tutor, 28, 3235–3271.

Hadiwardoyo, S.A., Patra, S., Calafate, C.T., Cano, J.-C., Manzoni, P., 2018. An intelligent transportation system application for smartphones based on vehicle position advertising and route sharing in vehicular ad-hoc networks. J Comput Sci Technol, 33, 249–262.

iiMedia Research, 2024. Research data on the development and user profiles of China's mobile map industry. https://data.iimedia.cn/data-classification/theme/13594741.html

Jiang, X., Li, M., Liu, Q., 2026. Joint longitudinal-lateral trajectory planning for CAVs in mixed traffic at signalized intersections. Commun Transp Res, 6, 9640011.

Jing, X., Pei, X., Yan, S., Han, C., Selpi, Andreotti, E., et al., 2022. Safety benefit of cooperative control for heterogeneous traffic on-ramp merging. Transport Saf Environ, 4, tdac031.

Lee, D., Lee, S., Chen, Z., Park, B.B., Shim, D.H., 2021. Design and field evaluation of cooperative adaptive cruise control with unconnected vehicle in the loop. Transport Res C-Emer, 132, 103364.

Lee, J.W., Wang, H., Jang, K., Lichtlé, N., Hayat, A., Bunting, M., et al., 2025. Traffic control via connected and automated vehicles (CAVs): An open-road field experiment with 100 CAVs. IEEE Control Syst, 45, 28–60.

Li, H., Sun, X., Zhuang, C., Li, X., 2025. On the robotic uncertainty of fully autonomous traffic: From stochastic car-following to mobility–safety trade-offs. Transport Res C-Emer, 178, 105254.

Li, S., Zhou, B., Xu, M., 2023. Analysis and improvement of car-following stability for connected automated vehicles with multiple information uncertainties. Appl Math Model, 123, 790–809.

Li, S., Zhou, B., Wang, T., Cheng, C., Xu, M., 2024a. Effects of uncertain anomalous information on traffic flow of automated vehicles with V2V communication. Physica A, 653, 130107.

Li, S., Zhou, B., Xu, M., 2024b. Modeling and analysis of traffic flow with automated vehicles affected by information deviations. Nonlinear Dyn, 112, 18099–18119.

Li, S., Zhou, B., Xu, M., 2024c. Unraveling the platoon dynamics of connected automated vehicles with information errors. IEEE Trans Intell Transp Syst, 25, 17260–17278.

Liang, Z., Pang, M., 2024. A variable time headway model for the mixed car-following process considering multiple front vehicles information in foggy weather. Transport Saf Environ, 6, tdae011.

Lim, Q., Lim, Y., Muhammad, H., Tan, D.W.M., Tan, U.-X., 2021. Forward collision warning system for motorcyclist using smart phone sensors based on time-to-collision and trajectory prediction. J Intell Connect Veh, 4, 93–103.

Liu, Z.S., Liu, Z.Y., Meng, Z., Yang, X., Pu, L., Zhang, L., 2016. Implementation and performance measurement of a V2X communication system for vehicle and pedestrian safety. Int J Distrib Sens Netw, 12, 155014771667126.

Long, K., Liang, Z., Shi, H., Shi, L., Chen, S., Li, X., 2024. Traffic oscillation mitigation with physics-enhanced residual learning (PERL)-based predictive control. Commun Transp Res, 4, 100154.

Lusvarghi, L., Grazia, C.A., Klapez, M., Casoni, M., Merani, M.L., 2023. Awareness messages by vulnerable road

Just Accepted

users and vehicles: Field tests via LTE-V2X. IEEE Trans Intell Veh, 8, 4418–4433.

Ma, G., Sun, B., Cheng, Z., Yang, W., Zhou, H., Liu, Q., et al., 2026a. Investigating the formation mechanism of merging/diverging collision risk in short weaving segments: An integrated approach using spatial-temporal risk field and explainable machine learning. Transport Res A-Pol, 209, 105017.

Ma, G., Sun, B., Yang, W., Yao, Z., 2026b. 1D and 2D trajectory optimization in weaving segments under a unified risk field framework: Cooperative merging control strategy towards mixed traffic environment. Transport Res B-Meth, 211, 103505.

Meneguette, R., De Grande, R., Ueyama, J., Filho, G.P.R., Madeira, E., 2023. Vehicular edge computing: Architecture, resource management, security, and challenges. ACM Comput Surv, 55, 1–46.

Ministry of Industry and Information Technology of the People's Republic of China, 2019. China automotive test cycle—Part 1: Light-duty vehicles. GB/T 38146.1-2019.

Oh, T., Kim, E.M., Nguyen, T.-T., Jeong, H., Choi, Y., Liebe, L., et al., 2026. Scalable and interoperable C-V2X framework for real-time intelligent decision support in autonomous mobility. Commun Transp Res, 6, 9640001.

Papoulis, A., Pillai, S.U., 2002. Probability, Random Variables, and Stochastic Processes. 4th edn. New York: McGraw-Hill.

Qin, Y., Wang, H., 2021. Analytical framework of string stability of connected and autonomous platoons with electronic throttle angle feedback. Transportmetrica A, 17, 59–80.

Research In China, 2025. Vehicle-road-cloud integration and C-V2X industry research report, 2025. https://www.researchinchina.com/Report/ShowReport.aspx?id=77095

Specht, M., 2021. Consistency of the empirical distributions of navigation positioning system errors with theoretical distributions—comparative analysis of the DGPS and EGNOS systems in the years 2006 and 2014. Sensors, 21, 31.

Speiran, J., Shakshuki, E.M., 2022. A smartphone VANET based forward collision detection system. In: Proceedings of the 12th International Conference on Emerging Ubiquitous Systems and Pervasive Networks, 33–42.

Sui, H., Zhang, J., Dai, X., 2024. Exponential mean-square string stability of vehicular platoon with stochastic disturbance and time delay. Int J Robust Nonlinear Control, 34, 5484–5504.

Sun, Jie, Zheng, Z., Sharma, A., Sun, Jian, 2023. Stability and extension of a car-following model for human-driven connected vehicles. Transport Res C-Emer, 155, 104317.

Teunissen, P.J.G., 2020. Best integer equivariant estimation for elliptically contoured distributions. J Geod, 94, 82.

Treiber, M., Kesting, A., 2013. Traffic Flow Dynamics: Data, Models and Simulation. Berlin: Springer Berlin Heidelberg.

U.S. Department of Transportation, 2024. USDOT releases national deployment plan for vehicle-to-everything (V2X) technologies to reduce death and serious injuries on America's roadways. https://www.transportation.gov/briefing-room/usdot-releases-national-deployment-plan-vehicle-everything-v2x-technologies-reduce

Wang, L., Lai, Y., Duan, Y., Mu, S., Li, X., 2023. V2I-aided platooning systems with delay awareness. IEEE Syst J, 17, 4671–4682.

Wen, W., Pfeifer, T., Bai, X., Hsu, L.-T., 2021. Factor graph optimization for GNSS/INS integration: A comparison with the extended Kalman filter. Navigation, 68, 315–331.

Wu, C., Cai, Z., He, Y., Lu, X., 2024. A review of vehicle group intelligence in a connected environment. IEEE Trans Intell Veh, 9, 1865–1889.

Xia, X., Meng, Z., Han, X., Li, H., Tsukiji, T., Xu, R., et al., 2023. An automated driving systems data acquisition and analytics platform. Transport Res C-Emer, 151, 104120.

Yan, P., Xia, X., Brizzi, M., Wen, W., Hsu, L.-T., 2025. Subspace-based adaptive GMM error modeling for fault-aware pseudorange-based positioning in urban canyons. IEEE Trans Intell Veh, 10, 3222–3237.

Yang, W., Sun, B., Ma, G., Sun, H., 2026. Car-following modeling with multi-model driving assistance and stability analysis under heterogeneous time delay. Chaos Solitons Fractals, 204, 117679.

Zhao, Y., Hua, X., Yu, W., Lin, W., Wang, W., Zhou, Q., 2025. Safety and efficiency-oriented adaptive strategy controls for connected and automated vehicles in unstable communication environment. Accid Anal Prev, 220, 108121.

Zhou, B., Li, S., Wang, S., Xu, M., 2025. Analysis of stability and cooperation in traffic flow with connected automated vehicles under perceptual uncertainty. Chaos Solitons Fractals, 199, 116745.

Zimmer, W., Wardana, G.A., Sritharan, S., Zhou, X., Song, R., Knoll, A.C., 2024. TUMTraf V2X cooperative perception dataset. In: Proceedings of the 2024 IEEE/CVF Conference on Computer Vision and Pattern Recognition (CVPR), 22668–22677.

Just Accepted

Author biography

Baofeng Sun received the B.S. degree from Jilin University of Technology, Changchun, China, in 1992, and the M.S. and Ph.D. degrees from Jilin University (JLU), Changchun, China, in 1999 and 2002, respectively. She is currently a Professor of Traffic Information Engineering and Control in JLU. Her research interests include behavior analysis of connected and automated vehicles, spatiotemporal data analysis and intelligent mobility services, and intelligent logistics system planning and operations optimization.

Wenyu Yang received the B.S. degree from Northeast Forestry University, Harbin, China, in 2024. He is currently pursuing the M.S. degree at Jilin University, Changchun, China. His research interests include connected and automated vehicles and intelligent transportation systems.

Guodong Ma received the B.S. degree from Shandong University of Science and Technology, Qingdao, China, in 2022. He is currently pursuing the Ph.D. degree at Jilin University, Changchun, China. His research interests include intelligent transportation systems, connected and automated vehicles, and model-data hybrid-driven optimization.

Xiaoxiang Na received the B.S. and M.S. degrees from Jilin University, Changchun, China, in 2007 and 2009, respectively, and the Ph.D. degree from the Department of Engineering, University of Cambridge (CUED), Cambridge, U.K., in 2014. He is currently a University Assistant Professor in applied mechanics with CUED. His research interests include driver-vehicle dynamics, in-service monitoring of road freight operations, and evaluation and modeling of energy performance of heavy goods vehicles.

Just Accepted